Iterative Model-Based Beamforming for High Dynamic Range Applications

Siegfried Schlunk, *Graduate Student Member, IEEE*, Kazuyuki Dei, and Brett Byram, *Member, IEEE*

***Abstract*— Clutter produced using bright acoustic sources can obscure weaker acoustic targets, degrading the quality of the image in scenarios with high dynamic ranges. Many adaptive beamformers seek to improve image quality by reducing these sidelobe artifacts, generating a boost in contrast ratio or contrast-to-noise ratio. However, some of these beamformers inadvertently introduce a dark region artifact in place of the strong clutter, a situation that occurs when both clutter and the underlying signal of interest are removed. We introduce the iterative aperture domain model image reconstruction (iADMIRE) method that is designed to reduce clutter while preserving the underlying signal. We compare the contrast ratio dynamic range (CRDR) of iADMIRE to several other adaptive beamformers plus delay-and-sum (DAS) to quantify the accuracy and reliability of the reported measured contrast for each beamformer over a wide range of contrast levels. We also compare all beamformers in the presence of bright targets ranging from 40 to 120 dB to observe the presence of sidelobes. In cases with no added reverberation clutter, iADMIRE had a CRDR of 75.6 dB when compared with the next best method DAS with 60.8 dB. iADMIRE also demonstrated the best performance for levels of reverberation clutter up to 0-dB signal-to-clutter ratio. Finally, iADMIRE restored underlying speckle signal in dark artifact regions while suppressing sidelobes in bright target cases up to 100 dB.**

***Index Terms*— Array signal processing, clutter, dynamic range, image quality, imaging, ultrasonic imaging.**

I. Introduction

ADAPTIVE beamforming methods have become increasingly popular in recent years due to the reportedly great improvements to contrast ratio or contrast-to-noise ratio (CNR) that they can produce [1]–[3]. However, there is growing concern that not all of these methods produce "true" improvements to contrast ratio and CNR. Because of this concern, some groups have begun expressing the importance of developing new robust measurements to test performance [4]–[8]. These methods include contrast ratio dynamic range (CRDR) [5], which seeks to quantify measured versus true contrast, and generalized CNR (GCNR) [6], [7], which seeks to generalize CNR by providing a detectability metric that is less susceptible to artificial improvements.

Many adaptive beamformers characterize their performance based on the contrast ratio of anechoic cysts, where the average target intensity is compared to some nearby background region. However, sidelobe clutter as well as the dark region artifact described by Rindal *et al.* [9] can interfere with this assessment. The dark region artifact can arise in the presence of strong acoustic targets, where sidelobe clutter will obscure nearby, lower strength acoustic targets. Some adaptive beamformers will remove this clutter, but in doing so also remove the underlying signal of interest, resulting in the dark region artifact. This lowers the intensity in that region leading to a reported contrast ratio or CNR that is higher than its true value. Alternatively, other beamformers may fail to remove this sidelobe clutter, resulting in cysts of varying intensities appearing identical (e.g., an anechoic cyst measured as −40 dB), as demonstrated by Dei *et al.* [5] with CRDR.

We provide several instances where these problems can occur clinically. First, renal cysts are quite common and are classified as either simple (benign, homogeneous, fluid-filled with a well-defined outline) or complex (indicative of disease, filled with nonhomogeneous fluid and an irregular cyst wall with potential calcifications) [10]. However, complex cysts can be difficult to classify [11], [12], and many beamformers will display a −40-dB complex cyst identically to a anechoic simple cyst, either due to removing the weak signal from the complex cyst or failing to remove the sidelobe clutter from the simple cyst. A second example is the visibility of blood flow. Because the blood signal is typically much weaker than the surrounding tissue signal, this can lead to the blood signal being completely masked by sidelobe clutter, or worse the blood signal being completely removed along with the clutter.

Since the dark region artifact can appear in situations where nearby targets have severe differences in acoustic strength, it is an important consideration for high dynamic range applications. In previous papers, we introduced the aperture domain model image reconstruction (ADMIRE) method [13]–[15] that uses a physics-based model to reduce strong sidelobe clutter and reverberation, which increased the dynamic range [5]. However, it is susceptible to the dark region artifact [16],

Manuscript received May 2, 2020; accepted July 22, 2020. Date of publication July 27, 2020; date of current version February 24, 2021. This work was supported in part by NIH under Grant R01EB020040 and Grant S10OD016216-01 and in part by the NSF under Award IIS-1750994. *(Corresponding author: Siegfried Schlunk.)*

Siegfried Schlunk and Brett Byram are with the Department of Biomedical Engineering, Vanderbilt University, Nashville, TN 37232 USA (e-mail: siegfried.g.schlunk@vanderbilt.edu).

Kazuyuki Dei was with the Department of Biomedical Engineering, Vanderbilt University, Nashville, TN 37232 USA. He is now with GE Healthcare, Wauwatosa, WI USA.

Digital Object Identifier 10.1109/TUFFC.2020.3012165

where the strong sidelobe clutter signal is preferentially fit by the model, resulting in the complete loss of the weaker underlying signal. In this article, we introduce iterative ADMIRE (iADMIRE) as a solution to that problem. In iADMIRE, sources of clutter are iteratively solved and subtracted from the input signal so that weaker signals can progressively be fit. This results in a more accurate estimate of the region of interest (ROI). We will show that this iterative approach can mitigate both sidelobe and dark region artifacts, improving CRDR in some cases.

II. Beamforming Algorithms

We include a brief explanation of ADMIRE to provide context for iADMIRE. Additionally, several other adaptive beamformers are described for comparison, since many of these beamformers are susceptible to sidelobe artifacts, dark region artifacts, or both. All beamformers are implemented in MATLAB (The MathWorks, Natick, MA, USA).

A. ADMIRE

ADMIRE is a method for removing reverberation and off-axis clutter, as well as suppressing wavefront aberration. Byram *et al.* [13] presented a detailed explanation of the components of the algorithm, and additional information can be found elsewhere [14], [15], but we include a cursory explanation here.

Processing begins by applying dynamic receive delays to the channel data. This delayed data is then divided into multiple overlapping windows along the axial dimension, along which the Fourier transform is performed [i.e., a short-time Fourier transform (STFT)]. This data can then be analyzed for each primary frequency component using a physics-based model. This model is the root of ADMIRE and is derived from the well-defined physics of linear wave propagation. It is composed of the predicted aperture domain signals created from scatterers throughout the field-of-view of the transducer, as defined by the equation

$$p_s(x;t,\omega)=\sum_{n=0}^{N-1}A(x;x_n,z_n,\tau_n,\omega)e^{jk\tau(x;x_n,z_n,\tau_n)} \quad (1)$$

where x is the position along the aperture, t and ω specify the time and frequency for the signal, k is the corresponding wavenumber, N is the total number of scatterers arriving at the transducer at time t, and $\tau(x;x_n,z_n,\tau_n)$ is the wavefront delay for a signal received from (x_n,z_n) at time τ_n. It is noted that τ_n can be different from t so that subtle shifts in phase can be included in the model. Finally, $A(x;x_n,z_n,\tau_n,\omega)$ is the amplitude modulation across the aperture caused by the STFT windows and element sensitivity.

These modeled signals are combined into a model matrix, X, which allow for representing a given aperture domain signal, y, by its component sources, β, by

$$y=X\beta \quad (2)$$

where y is for a specific wavenumber k and location (x_n,z_n), X is the set of physical model predictors, and β the set of solved model coefficients. Fig. 1 is included to give an intuitive sense of how each signal in the model matrix X relates to a specific physical source location. In theory, solving (2) by multiplying by X^{-1} reveals the exact composition of β, which reveals the specific physical locations of the various reflected echoes that linearly combine to form y. For the current location being processed, ADMIRE then chooses some small ROI centered at that location and can simply remove the coefficients for sources outside of that ROI, and reconstruct the decluttered signal as

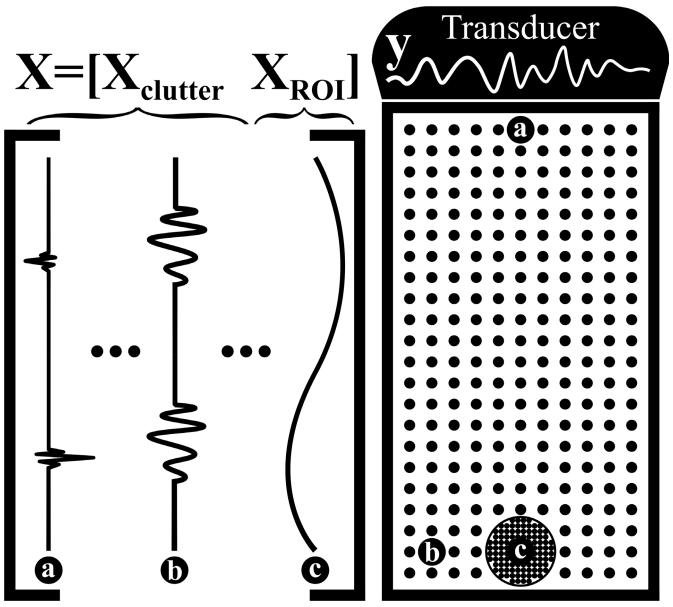

Fig. 1. Example model X, composed of a set of estimated signals from locations considered to be clutter (sparsely sampled, e.g., a and b), and a set from locations considered to be ROI (highly sampled, e.g., c). For a given aperture domain signal y, the model can be used to estimate which sources are components of the received signal, thus removing the signal components that are not from the ROI.

$$y_{\text{decluttered}}=X\beta_{\text{ROI}} \quad (3)$$

using only the coefficients β_{ROI} corresponding to signals originating from inside the ROI. This removes any signals located off-axis or from reverberant sources.

In practice, (2) is ill-posed due to the relatively small size of y compared to the potentially large size of X depending on the sampling of the model space. To solve for the model predictors, ADMIRE uses the elastic-net regularization technique [17] with the optimization equation

$$\hat{\beta}=\arg\min_{\beta}\left(||y-X\beta||^2+\lambda\left(\alpha||\beta||_1+(1-\alpha)||\beta||_2^2/2\right)\right) \quad (4)$$

where $||\beta||_1$ is the L1 norm, $||\beta||_2$ is the L2 norm, and α is set between 0 and 1 to control the weighting between L1 and L2. λ is a regularization parameter which controls the degrees of freedom [18]. Choosing $\alpha=1$ results in a purely L1 fit, resulting in high coefficient sparsity and little (or no) correlation between them. Setting $\alpha=0$ is L2 and results in almost no nonzero coefficients, with many of the coefficients being correlated. L1 and L2 both have benefits and shortcomings, and the elastic-net allows for a balanced

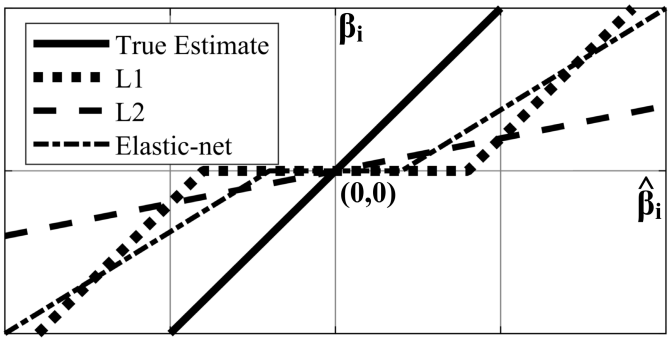

Fig. 2. Qualitative example of the L1, L2, and elastic-net estimates for some specific model coefficient, β_i. In the L1 case, coefficients that are sufficiently small are zeroed in favor of larger ones. No coefficients are zeroed in L2, but instead there is significant coefficient shrinkage (loss of amplitude) for stronger components. ADMIRE uses the elastic-net, which balances the two extremes but includes features of both.

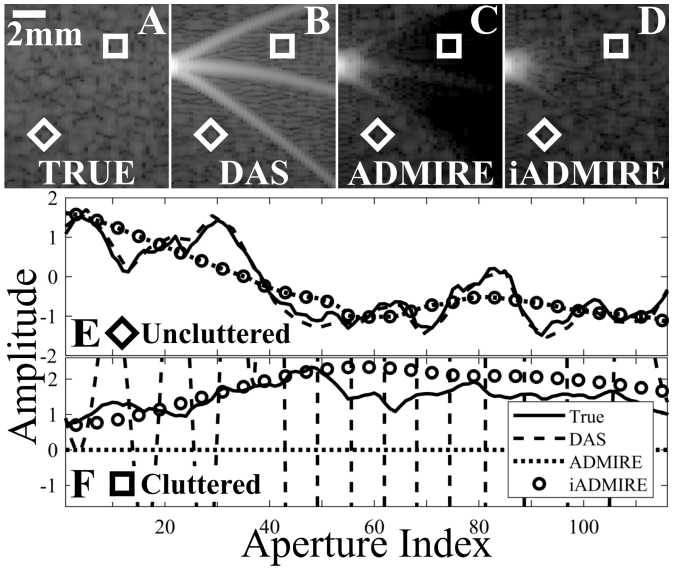

Fig. 3. Example of the effect of iADMIRE on the dark region artifact. (a) DAS showing the uncluttered, True speckle background. (b) DAS of the same background with a simulated 100-dB bright scatterer introducing strong sidelobe clutter. (c) ADMIRE and (d) iADMIRE processing of the scatterer. ADMIRE demonstrates sidelobe reduction with a visible dark region artifact, and iADMIRE shows the same reduction without the artifact. (e) Aperture domain signals for the uncluttered region denoted by the diamond. (f) Signals for the cluttered region denoted by the square. When no clutter is present, ADMIRE and iADMIRE match the True and DAS signals since there is no clutter to be removed (note that the slight difference in signal is due to the sparse fitting of coefficients and has marginal impact on the final image). With sidelobe clutter present, ADMIRE removes all signal in the region, while iADMIRE is able to restore the underlying signal.

minimization between the two. In this article, we choose $\alpha = 0.9$ and λ based on the root mean square (rms) of the signal y. We ran both a low degree of freedom (LDF) and a high degree of freedom (HDF) case, giving us $\lambda_{\text{LDF}} = (0.0189/2)y_{\text{rms}}$ and $\lambda_{\text{HDF}} = (0.0189/10)y_{\text{rms}}$. Generally, higher degrees of freedom result in a more precise fit with many more nonzero coefficients, while lower degrees of freedom favor sparsity of coefficients. The choice of parameters is based on previous work [13], [14], and in our testing seems to be robust across most imaging scenarios.

Once the aperture domain signal has been decluttered using the coefficients solved by the elastic-net and (3), the inverse STFT is applied to return to the time domain [19]. This results in a decluttered version of the channel data that can still be processed using other beamformers, if desired, or simply combined using the delay-and-sum (DAS) equation (7). In this article, the ADMIRE results do not include any additional postprocessing. Computation time is variable since it increases at deeper depths (larger models), for larger apertures, and for increased overlap between STFT windows. For the simulations in this article, we use 90% overlap between windows and process a 10-mm band centered at a depth of 3 cm. This was split across 50 computational cores, with each core requiring 30–40 min. Though this timing is acceptable for research, a variety of ADMIRE development efforts are focused on architectural changes to achieve near real-time processing [20].

B. iADMIRE

iADMIRE is a modification to the ADMIRE algorithm that seeks to accommodate environments with high dynamic ranges by mitigating the shortcomings of the elastic-net [21]. To provide some intuition for these problems, we include in Fig. 2, an example of how L1, L2, and elastic-net regularizations affect the estimate of a given coefficient. With an L1 estimate, coefficients that are sufficiently small will be ignored and set to zero, but larger coefficients will be fit relatively accurately, leading to coefficient selection. With L2, no coefficients are lost, but the cost is that larger coefficients undergo severe shrinkage and are underestimated. By incorporating characteristics of both, the elastic-net seeks to minimize the negatives of each method, but crucially does not eliminate them. Since ADMIRE uses the elastic-net and therefore has L1 features, we see that weaker signal components may be zeroed out in favor of stronger sources. This can result in a dark region artifact since only the strong clutter coefficients are fit, resulting in nothing from the ROI being included. Fig. 3 shows an example of a speckle background (A) that is corrupted by a 100-dB scatterer (B) and highlights an uncluttered region (diamond) and a cluttered region (square). For the uncluttered region, the aperture domain signals for all four match closely since there is no clutter interference (note that the small differences between the DAS and ADMIRE signals is due to the elastic-net estimates of ADMIRE favoring the dominant signal components, and has little impact on the actual image). In contrast, the DAS signal in the cluttered region is completely different due to the sidelobe clutter, and ADMIRE predominantly fits that clutter resulting in a loss of the underlying signal and the creation of the dark region artifact. iADMIRE, however, first fits and removes that clutter signal, allowing it to recover the true underlying signal.

Algorithm 1 shows the process by which iADMIRE iteratively solves for the clutter sources in the signal and removes them, theoretically obtaining a more accurate estimate of the ROI signal. Rather than doing a single solve for the model coefficients and reconstructing only the ROI signal, iADMIRE computes the clutter-only signal y_{clutter} using (5) and the coefficients β_{clutter} corresponding to the clutter predictors in the model and subtracts that from the original signal with (6).

Algorithm 1 Iterative Clutter Removal in ADMIRE

Given model predictors $X = [X_{\text{ROI}} X_{\text{clutter}}]$, aperture domain signal y_1, parameters α and λ, and $\delta > 0$
for $i = 1$ **do**
Solve (4) for model coefficients $\hat{\beta}_i$, given y_i, X
Compute clutter-only signal

$$y_{i,\text{clutter}} = X_{\text{clutter}} \hat{\beta}_{i,\text{clutter}} \tag{5}$$

Compute new aperture signal

$$y_{i+1} = y_i - y_{i,\text{clutter}} \tag{6}$$

Stop when $||y_{i+1} - y_i||_2^2 < \delta$
end for
Calculate $y_{\text{decluttered}} = X_{\text{ROI}} \hat{\beta}_{i,\text{ROI}}$

By iteratively applying the elastic-net and removing the reconstructed clutter signal from the signal, strong clutter sources are continually removed until some threshold is reached. This new, less cluttered signal is then decomposed using the elastic-net one last time to produce the decluttered signal using (3).

We set $\delta = \max(\text{abs}(y))/1000$ so that convergence will depend on the input aperture domain signal. Fig. 4 shows a simple example of convergence for a dark artifact region. At zero iterations (normal ADMIRE), the dark region artifact is clearly visible, but after a single iteration the background appears to be mostly restored. Based on the change in power between iterations, the algorithm has functionally converged by the third iteration. For simple clutter scenarios where there is one main source of interference, it is likely that only one or a few iterations is required to remove that source. As a result, for this study we enforce a hard cutoff of three iterations to prevent wasted computation time. For ease of comparison, the other parameters that overlap with the standard ADMIRE algorithm are the same as those for ADMIRE (HDF) in Section II-A. The balance between L1 and L2 fitting could be further tuned to adjust convergence and clutter removal, however, we have found that these values provide a fairly good balance to prevent overfitting (and failing to remove clutter) or underfitting (requiring more iterations).

Computation time for iADMIRE varies wildly depending on the number of iterations required. Since the elastic-net decomposition is computationally expensive, a window that requires many iterations (and therefore many repeated fits) needs nearly that much additional processing time. As a result, for any given signal being fit, it can take between one and three times as long to process as standard ADMIRE.

C. DAS

The conventional DAS signal for an image pixel can be defined as

$$S_{\text{DAS}}(x, z) = \sum_{i=1}^{M} w_i(z) s_i(x, z) \tag{7}$$

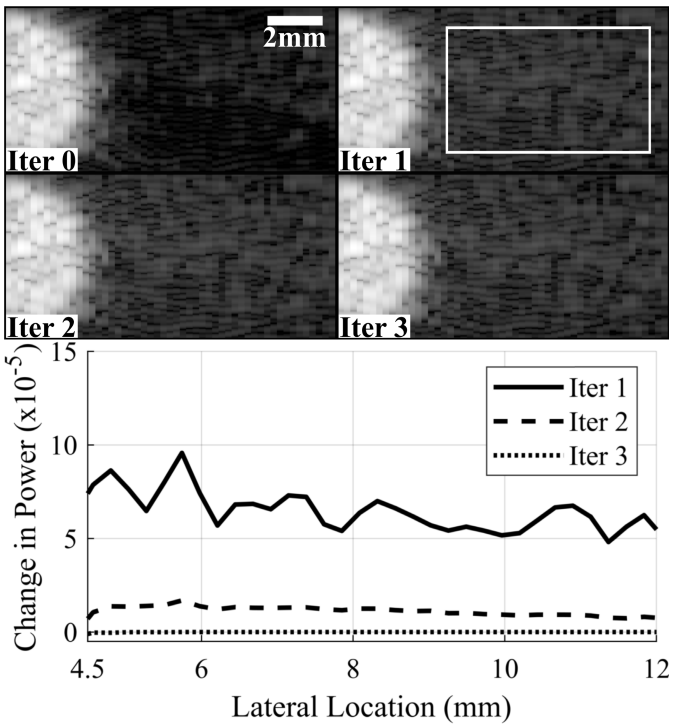

Fig. 4. Example of iADMIRE after 0, 1, 2, and 3 iterations for a 60-dB cyst. The change in power between iterations of the indicated region is included. At 0 iterations (normal ADMIRE) the dark region artifact is clearly visible, but is almost entirely mitigated after the first iteration. In this example, iADMIRE has mostly converged by the third iteration.

where x is the a-line of the final image, z is a discrete time index, M is the total number of channels, $w_i(z)$ is the weighting factor for channel i, and $s_i(x, z)$ is the delayed signal across the aperture for a given channel i. The weighting factor accounts for apodization, and can vary by depth and channel (taking F-number into consideration) or be static as in the case of a fixed rectangular window, where all channels are weighted equally. In this study, we use rectangular weighting, unless otherwise specified.

D. Filtered Delay-Multiply-and-Sum (F-DMAS)

F-DMAS

is a simple adaptive beamformer proposed to improve contrast and resolution [1]. It works by combinatorially coupling and multiplying the delayed channel data before summing across the channels. The unfiltered DMAS signal can be calculated as

$$\mathbf{S}^*_{\text{DMAS}}(z) = \sum_{i=1}^{M-1} \sum_{j=i+1}^{M} \hat{\mathbf{s}}_{ij}(z) \tag{8}$$

and $\hat{\mathbf{s}}_{ij}(z)$ is defined as

$$\hat{\mathbf{s}}_{ij}(z) = \text{sign}(\mathbf{s}_i(z)\mathbf{s}_j(z)) \sqrt{|\mathbf{s}_i(z)\mathbf{s}_j(z)|}. \tag{9}$$

The filtered signal can then be calculated from $\mathbf{S}^*_{\text{DMAS}}$ by removing the dc and high-frequency components using a bandpass filter centered around $2f_c$.

E. Generalized Coherence Factor (GCF)

GCF is a weighting of the DAS image by the ratio of the energy in some low-frequency region to the total energy [2]. This ratio for a pixel at (x, z) is defined as

$$\mathrm{GCF}(x,z) = \frac{\sum_{k=0}^{M_0} |P_k(x,z)|^2}{\sum_{k=0}^{M} |P_k(x,z)|^2} \tag{10}$$

where M is the number of channels, M_0 is the chosen cutoff frequency index, and $P(k)$ is the M-point discrete Fourier transform across the aperture as defined by

$$P_k(x,z) = e^{j\pi k} \sum_{i=0}^{M} s_i(x,z) e^{-j2\pi(ik/M)} \tag{11}$$

where $s_i(x, z)$ is the delayed channel data for channel i. GCF allows us to vary between pure coherence factor ($M_0 = 0$) and DAS ($M_0 = M$). We chose $M_0 = 5$ as done in [9]. The final GCF image is then calculated simply as

$$S_{\mathrm{GCF}}(x,z) = \mathrm{GCF}(x,z) S_{\mathrm{DAS}}(x,z). \tag{12}$$

F. Minimum Variance (MV)

MV beamforming is also an adaptively weighted DAS image, where the optimized apodization weights [22], [23] are

$$\mathbf{w} = \frac{R^{-1}\mathbf{e}}{\mathbf{e}^H R^{-1}\mathbf{e}} \tag{13}$$

where $\mathbf{e}$ is the steering vector, H is the conjugate transpose, and R is the covariance matrix defined as

$$R(z) = E[\mathbf{s}(z)\mathbf{s}(z)^H] \tag{14}$$

where E[·] denotes the expectation and $\mathbf{s}(z)$ is the delayed aperture signal at depth z. To get an invertible matrix, we used subarray lengths of L, equal to 50% of the total aperture length, to estimate the covariance matrix and diagonal loading defined as $\epsilon = \Delta \cdot \mathrm{tr}(\hat{R})$, where $\Delta = 1/(10L)$, as recommended [23]. The MV signal estimate is then defined as

$$\hat{\mathbf{S}}_{\mathrm{MV}}(z) = \frac{1}{M-L+1} \sum_{l=0}^{M-L} \mathbf{w}(z)^H \bar{\mathbf{s}}(z) \tag{15}$$

where M is the total aperture length and $\bar{\mathbf{s}}(z)$ is the delayed aperture signal for the corresponding subarray.

G. Short-Lag Spatial Coherence (SLSC)

SLSC is different from many other beamformers in that it only uses the spatial coherence of received echoes to form images. The coherence images are usually displayed on a linear scale. Introduced by Lediju *et al.* [24], the foundation of SLSC is the van Citter-Zernike (VCZ) theorem, which demonstrates a prediction for the spatial coherence, or covariance, for the backscattered echoes [25]. SLSC is computed per pixel using a correlation kernel as

$$S_{\mathrm{SLSC}}(x,z) = \sum_{l=1}^{L} \frac{1}{M-l} \sum_{i=1}^{M-l} \frac{\sum_{n=z}^{z+n_k} s_i(x,n) s_{i+l}(x,n)}{\sqrt{\sum_{n=z}^{z+n_k} s_i^2(x,n) \sum_{n=z}^{z+n_k} s_{i+l}^2(x,n)}} \tag{16}$$

TABLE I
FIELD II SIMULATION PARAMETERS FOR CONTRAST TARGET PHANTOMS

Parameter	Value
Number of elements	117
Number of mathematical elements (lateral)	7
Number of mathematical elements (elevation)	11
Element height	4 mm
Element width	0.254 mm
Kerf	0.003 mm
Lateral pitch	0.257 mm
Center frequency (f_c)	3 MHz
Sampling frequency (simulation) (f_s)	640 Mhz
Sampling frequency (downsampled) (f_s)	40 MHz
Bandwidth	60%
Transmit focal depth	3 cm
Transmit/receive f-number	1

where l is the lag, L is the number of lags to sum, and n_k is the size of the correlation kernel. This produces an SLSC image calculated per a-line x and each depth z. The choice of number of lags is recommended as <30% of the total number of channels [26]. For this study, we chose to use $L = 20$ lags (17% of our total number of channels), with a correlation kernel equivalent to 1 wavelength.

H. Gray-Level Transformation (GLT)

For comparison purposes, we include the GLT that is described by Rindal *et al.* [8] as an example of a method that "fakes" improvements to CNR, but sacrifices the dynamic range. The GLT is a sigmoid function defined as

$$\hat{S}_{\mathrm{GLT}}(B) = \frac{1}{1+e^{-\alpha(B-\beta)}} \tag{17}$$

$$S_{\mathrm{GLT}}(B) = \frac{\hat{S}_{\mathrm{GLT}}(B) - \max(\hat{S}_{\mathrm{GLT}}(B))}{\epsilon} \tag{18}$$

where $B = 20\log_{10}(|S_{\mathrm{DAS}}|)$, $\alpha = 0.12$, $\beta = -40$, and $\epsilon = 0.008$.

III. METHODS

A. Contrast Target Phantom

Field II [27], [28] was used to simulate 5-mm-diameter cysts of known contrasts ranging from −50 to 70 dB relative to the background, plus an anechoic case. Each level of contrast was simulated with six independent realizations of speckle. Simulation parameters used in Field II are detailed in Table I.

B. Simulated Reverberation Clutter

For each of the contrast phantoms, additional realizations were created that included simulated reverberation clutter. This reverberation clutter was simulated using the technique detailed by Byram and Shu [29], [30]. The clutter was added directly to the channel data such that it satisfied the signal-to-clutter ratio (SCR) calculated by

$$\mathrm{SCR} = 10\log_{10}\left(\frac{P_{\mathrm{SOI}}}{\alpha^2 P_{\mathrm{clutter}}}\right) \tag{19}$$

where P_{SOI} is the power of the channel data of the original phantom, P_{clutter} is the power of the channel data of the reverberation clutter, and α is the scalar for the reverberation clutter to achieve the desired SCR. A region of background was used to calculate the power for each phantom so that the amount of clutter added was consistent across the different magnitudes of cysts. Equation (19) can then be rewritten to solve for α as

$$\alpha = \sqrt{\frac{P_{\text{SOI}}}{P_{\text{clutter}} 10^{\text{SCR}/10}}}. \tag{20}$$

The scalar α is then calculated and the clutter channel data is scaled and combined with the phantom channel data. In this article, the reverberation clutter is scaled against the background speckle to achieve realizations with 20-, 10-, 0-, −10-, and −20-dB SCR compared to the channel data. We believe these values cover a realistic range of *in vivo* possibilities, though we expect most clinical cases probably fall between 20 dB (easy-to-image patients) and 0 dB (difficult-to-image patients). However, there is a significant lack of research into the quantification of reverberation, making it difficult to know the level of reverberation clutter for any given scenario. Some groups have investigated reverberation clutter, but mainly do so in the context of harmonic imaging [31], [32]. Studies involving the addition of simulated reverberation clutter fall within our simulated range [26], [32], and one *in vivo* study found that bladder images had bladder wall to clutter ratios between 30 and 0 dB for all sources of clutter including reverberation [33], further supporting our choice.

C. Bright Scatterer Phantom

To measure the dark region artifact, we used Field II to simulate bright point targets at the focal depth with contrasts ranging from 40 to 120 dB relative to the background speckle. As before, six speckle realizations were created for each amplitude. The same parameters found in Table I were used for simulation.

D. In Vivo Carotid Artery Data

We additionally captured *in vivo* carotid artery data from a healthy individual using a Verasonics Vantage Ultrasound System (Verasonics, Inc., Kirkland, WA, USA) with a L12-5 linear transducer. A center frequency of 7.813 MHz was used to acquire eight equally spaced angled plane waves spanning −9° to 9° at a PRF of 3000 Hz. Coherent compounding was used to generate a synthetically focused channel data set [34]. The resulting frames were processed using either ADMIRE or iADMIRE and filtered using a sixth-order Chebyshev filter with a cutoff frequency of 300 Hz to create a power Doppler (PD) image.

E. Contrast Ratio, CNR, and Resolution

The contrast ratio and CNR were measured for each phantom to characterize the measured contrast and detectability of the simulated cyst. Contrast ratio and CNR were defined as

$$\text{contrast ratio} = 20\log_{10}\left(\frac{\mu_{\text{ROI}}}{\mu_{\text{background}}}\right) \tag{21}$$

$$\text{CNR} = \frac{|\mu_{\text{ROI}} - \mu_{\text{background}}|}{\sqrt{\sigma^2_{\text{ROI}} + \sigma^2_{\text{background}}}} \tag{22}$$

where μ is the mean value and σ is the standard deviation of the enveloped, but not log compressed, data. Fig. 5 shows the chosen ROI and background regions for the contrast and bright scatterer phantoms. Additionally, the point spread function (PSF) was found for each bright scatterer and for each method. The mean point target width was measured across all scatterers (except 40 dB due to the noise floor) for each method at −6 dB (full width at half maximum), −10 dB, and −20 dB.

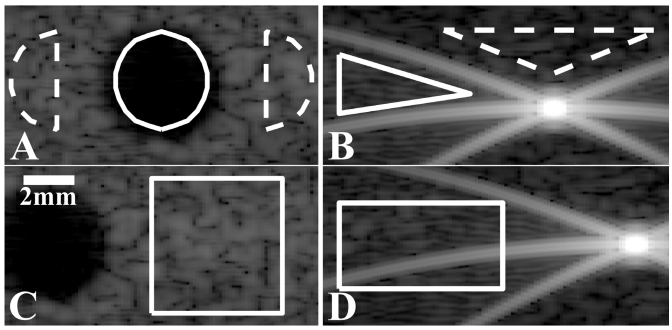

Fig. 5. DAS images for hypoechoic contrast target phantoms (left) and bright scatterer phantoms (right) simulated in Field II. (a) and (b) Target (solid) and background (dotted) regions used to calculate contrast ratio, CNR, and GCNR measurements. (c) and (d) Regions used for computing the background speckle correlation of each beamformer.

F. CRDR

In an effort to better characterize true contrast in beamformers, Dei *et al.* [5] proposed the CRDR method. By applying a given beamformer to simulated cysts at varying intensities, in this case ranging from −50 to 70 dB plus an anechoic cyst, the measured contrast can be compared to the true contrast over a wide range. For a given realization, the measured contrast is then linearly interpolated to get a well sampled curve. The CRDR measurement can then be estimated from that measured versus true contrast curve by determining the range on the curve for which the measured contrast does not deviate from the true contrast (two-tailed t-test, $\alpha = 0.05$).

G. GCNR

An alternative to CNR for measuring detection probability was proposed by Rodriguez-Molares *et al.* [6], [7] called the GCNR. It works by measuring the overlap of the probability density function between the ROI and the background, meaning it is unaffected by stretches or compressions in the dynamic range. The GCNR is then defined by

$$\text{GCNR} = 1 - \text{OVL} \tag{23}$$

where OVL is the measured overlap between the two probability density functions. Therefore, GCNR varies

TABLE II
CRDR FOR DIFFERENT LEVELS OF ADDED REVERBERATION CLUTTER

	Contrast ratio dynamic range (dB)				
Signal-to-clutter ratio (dB)	20	10	0	-10	-20
DAS	50.0	50.0	23.6	0.5	0.5
DAS - Hamming	60.8	60.8	23.3	1.7	1.6
DMAS	9.5	9.5	3.6	**13.0**	1.2
GCF	10.5	10.5	4.3	5.6	**7.4**
MV	10.9	10.9	5.7	2.9	2.9
SLSC	15.9	15.9	17.0	4.8	4.4
GLT	3.5	3.5	3.5	3.5	3.5
ADMIRE (LDF)	26.4	26.4	8.2	8.8	4.9
ADMIRE (HDF)	45.4	45.4	32.9	1.7	1.6
ADMIRE (HDF) - Hamming	46.8	46.8	30.7	2.9	2.6
iADMIRE	72.1	72.1	37.3	1.8	1.6
iADMIRE - Hamming	**75.6**	**75.6**	**41.4**	2.6	2.6

between 0 and 1, where GCNR = 1 indicates perfect discrimination. The GCNR is computed for the contrast target phantoms using the same ROI and background regions as for contrast ratio (Fig. 5).

H. Speckle Correlation

The 2-D correlation coefficient r was calculated by comparing each simulated phantom to its corresponding speckle realization in DAS (with no cyst or bright scatterer present) to determine the degree of speckle corruption from the sidelobe and dark region artifacts. The region used for the measurement is shown in Fig. 5. The correlation was calculated as

$$r = \frac{\sum_x \sum_z (S(x,z) - \mu_S)(D(x,z) - \mu_D)}{\sqrt{\left(\sum_x \sum_z (S(x,z) - \mu_S)^2\right)\left(\sum_x \sum_z (D(x,z) - \mu_D)^2\right)}} \tag{24}$$

where S is the enveloped, uncompressed region of the data for the beamformer of interest, and D is the short-hand for the reference DAS enveloped, uncompressed region of data. Values of r closer to 1 indicate more accurate speckle in the target region.

IV. RESULTS

A. Contrast Target Phantoms

The dynamic range for all beamformers in the presence of no added reverberation clutter and the computed CRDR for a range of SCRs is shown in Fig. 6. Since CRDR aims to quantify how accurately a beamformer represents contrast, a higher CRDR corresponds to a longer range over which a beamformer reports the true contrast. SLSC and GLT notably deviate from the true contrast line since they are designed to enhance CNR at the cost of CRDR, which they do as shown in Fig. 7(b). Table II shows the measured CRDR for all beamformers at each level of added reverberation clutter from 20 dB (very low clutter) to −20 dB (very high clutter). We also include versions of DAS, ADMIRE (HDF), and iADMIRE summed using Hamming apodization since DAS especially benefits in this scenario. Though this does significantly improve the CRDR for DAS, it still does not match the performance of iADMIRE, apodized or unapodized. Overall, for SCRs between 20 and 0 dB, iADMIRE continues to have the highest CRDR, but

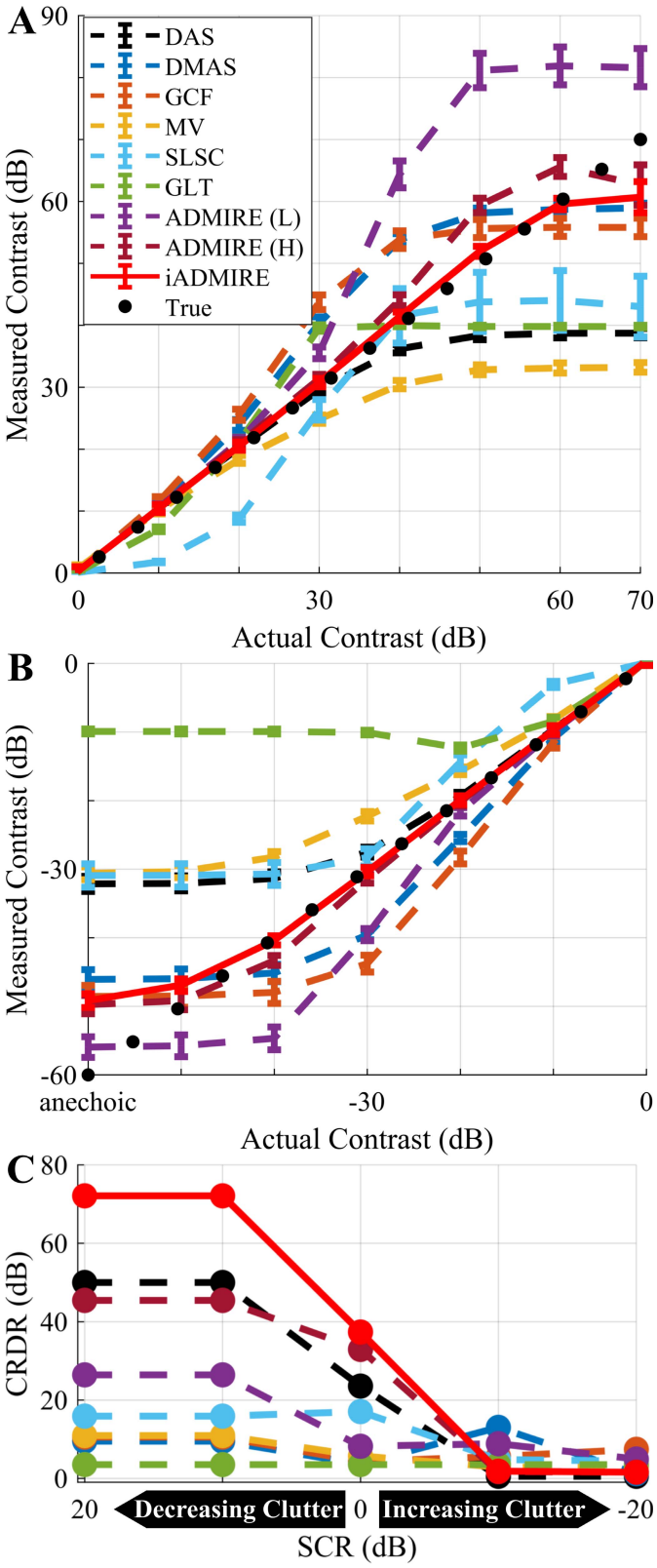

Fig. 6. Dynamic range displayed as measured contrast versus actual contrast for (a) hyperechoic and (b) hypoechoic cysts. The black-dotted line indicates the true contrast, and adherence to that line indicates more accurate reporting of measured contrast. (c) Computed CRDR for a range of SCR. Included error bars indicate the standard deviation.

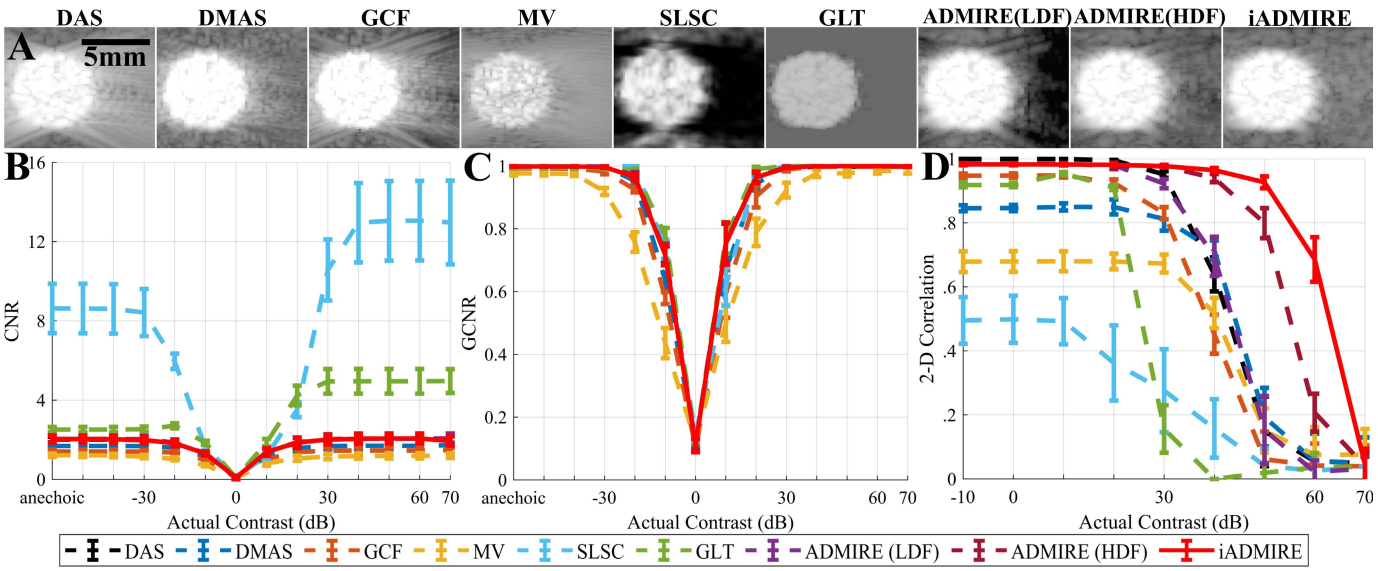

Fig. 7. (a) Sample realization of each beamformer for a 60-dB hyperechoic cyst. All beamformers are displayed on a 120-dB log scale to highlight the strong sidelobes (where present), except SLSC, which is displayed linearly, as is the convention. (b) CNR, (c) GCNR, and (d) 2-D speckle correlation calculated for the full range of cysts without added reverberation clutter. Included error bars indicate the standard deviation. Images are normalized so that background speckle is at the same level across methods.

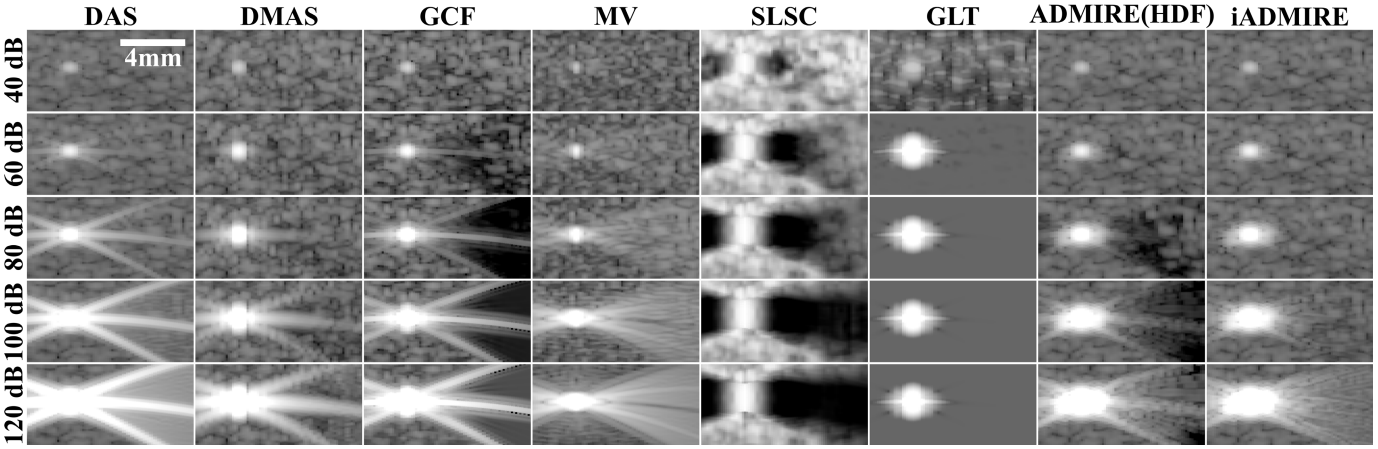

Fig. 8. Sample realization of bright scatterer phantoms at 40, 60, 80, 100, and 120 dB. All beamformers are displayed on a 100-dB log scale to highlight sidelobes and background speckle, except SLSC, which is displayed linearly, as is the convention. Images are normalized so that background speckle is at the same level across methods.

at more intense levels of reverberation all beamformers suffer poor CRDR.

One realization of a simulated 60-dB contrast target phantom without added reverberation clutter is shown in Fig. 7(a). The images are displayed on a compressed log scale of 120 dB to highlight the impact of the strong sidelobes. We can qualitatively see the sidelobe artifacts in DAS, DMAS, GCF, and MV, which has a noticeable affect on the dynamic range as shown. We can also see the affect that SLSC and GLT have on the background speckle near the cyst, which provides a great boost to CNR, as reported in Fig. 7(b). SLSC vastly outperforms the other methods due to this suppression of speckle in the background, with GLT performing second best for similar reasons. For all magnitudes of cysts, SLSC and GLT have better than or equal CNR to the other beamformers. In comparison, for GCNR shown in Fig. 7(c), all methods are fairly similar at all levels of contrast.

Fig. 7(d) shows the 2-D correlation coefficient of the defined speckle region for all beamformers at all contrast levels when compared with the corresponding speckle realization in DAS at 0 dB (no cyst), which should be the true speckle. Again, due to the suppression of speckle, SLSC and GLT have significantly reduced speckle accuracy, and all methods begin to lose accuracy at contrast levels greater than 30 dB due to the effect of the sidelobe artifact. In the low reverberation clutter cases, ADMIRE (HDF) has speckle accuracy above 0.90 for cysts up to 50 dB, and iADMIRE performs similar up to 60 dB. However, for increased levels of reverberation, all the methods are reduced to nearly 0 correlation as the reverberation clutter completely masks the original speckle.

B. Bright Scatterer Phantoms

A realization of the bright scatterer phantoms is shown in Fig. 8. Since ADMIRE (HDF) outperforms ADMIRE (LDF)

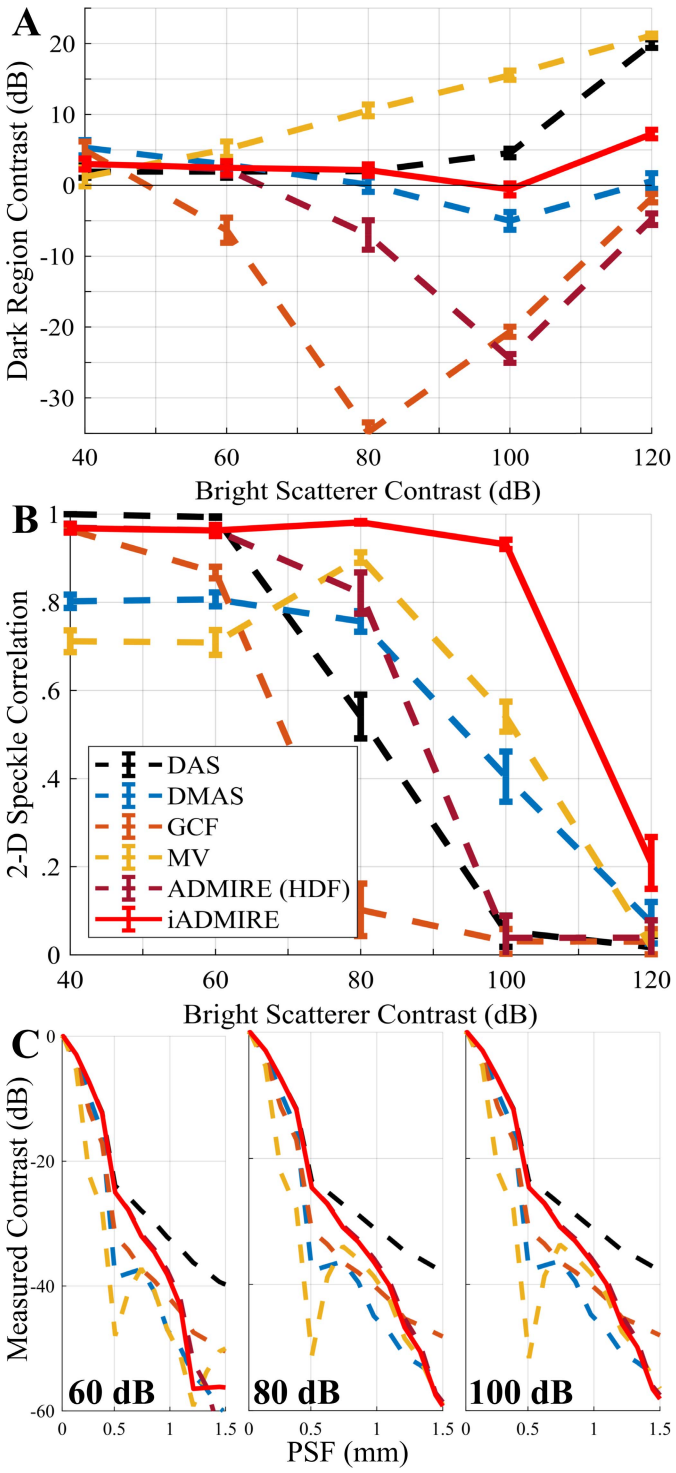

Fig. 9. (a) Contrast of the dark region artifact versus the strength of the simulated bright scatterer. Negative contrast indicates the presence of a dark region artifact, while positive contrast indicates strong sidelobe clutter. Values close to 0 dB indicate low artifact interference. (b) 2-D speckle correlation in the area of the dark region artifact as compared to clean background speckle. Values close to 1 indicate better speckle accuracy. (c) PSFs for the 60-, 80-, and 100-dB bright scatterers, displayed from the center of the target.

in terms of mitigating the dark region artifact, we have only included the better variation. Sidelobe artifacts are present in DAS, DMAS, GCF, and MV, and begin to show in ADMIRE at higher bright scatterer contrasts. The dark region artifact is strongly present in the GCF, SLSC, and ADMIRE images, and somewhat present in the DMAS images. GLT does not obviously exhibit either artifact, but that is primarily due to the background speckle being completely suppressed by the operation. iADMIRE shows reduction in the sidelobe artifacts, but also the removal of the dark region artifact and restoration of the background speckle in cases up to 100 dB.

TABLE III
MEAN POINT TARGET WIDTH AT VARYING LEVELS

	Point Target Width (mm)		
Intensity (dB)	-6 (FWHM)	-10	-20
DAS	0.49±.00	0.68±.00	0.94±.00
DMAS	0.45±.00	0.59±.00	0.77±.00
GCF	0.35±.00	0.49±.00	0.77±.00
MV	**0.23±.00**	**0.30±.00**	**0.49±.00**
SLSC	2.04±.00	2.48±.00	3.14±.01
GLT	0.82±.01	0.99±.01	1.52±.01
ADMIRE (HDF)	0.48±.01	0.68±.00	0.89±.00
iADMIRE	0.50±.01	0.68±.01	0.89±.01

Fig. 9(a) shows the contrast in the area of the dark region artifact compared to the uncorrupted background, and Fig. 9(b) shows the calculated speckle correlation for the area impacted by the two artifacts. As expected from the included realization, DMAS demonstrates improved contrast in the dark artifact region due to somewhat suppressed sidelobes and minimal dark region artifact, though iADMIRE has better overall artifact mitigation. For the 120-dB case, all beamformers demonstrated severe artifacts either due to sidelobes or the dark region artifact. Several methods have speckle accuracy greater than 0.75 for cases at or less than 80 dB, but only iADMIRE has accuracy above 0.90 in all cases up to 100 dB. Finally, Fig. 9(c) shows the PSF for a realization of the 60-, 80-, and 100-dB bright scatterers, and Table III shows the corresponding mean point target width. For all levels, ADMIRE and iADMIRE have comparable or better resolution compared to DAS, but MV consistently has the best resolution among the beamformers.

C. In Vivo Carotid Artery

The top row of Fig. 10 shows the B-mode of the carotid artery beamformed using DAS, ADMIRE (HDF), and iADMIRE, as well as a difference image to show the changes between DAS and iADMIRE. The middle rows show the white dashed line region enlarged and beamformed with rectangular and Hamming apodization to highlight the high clutter in DAS with rectangular apodization. ADMIRE (HDF) removes this clutter entirely, presenting a dark region artifact in the same location, and iADMIRE lessens the clutter and preserves some of the underlying speckle. The difference images show iADMIRE with rectangular apodization when compared with DAS with rectangular and Hamming apodization. Its is noted that the middle rows are displayed on a smaller dynamic range to make the changes between speckle and clutter more visible. Finally, a PD image is shown for each method.

V. DISCUSSION

A. Contrast Target Phantoms

The CRDR demonstrates the issue of saturation due to the interference of the sidelobe artifact, where cysts at different

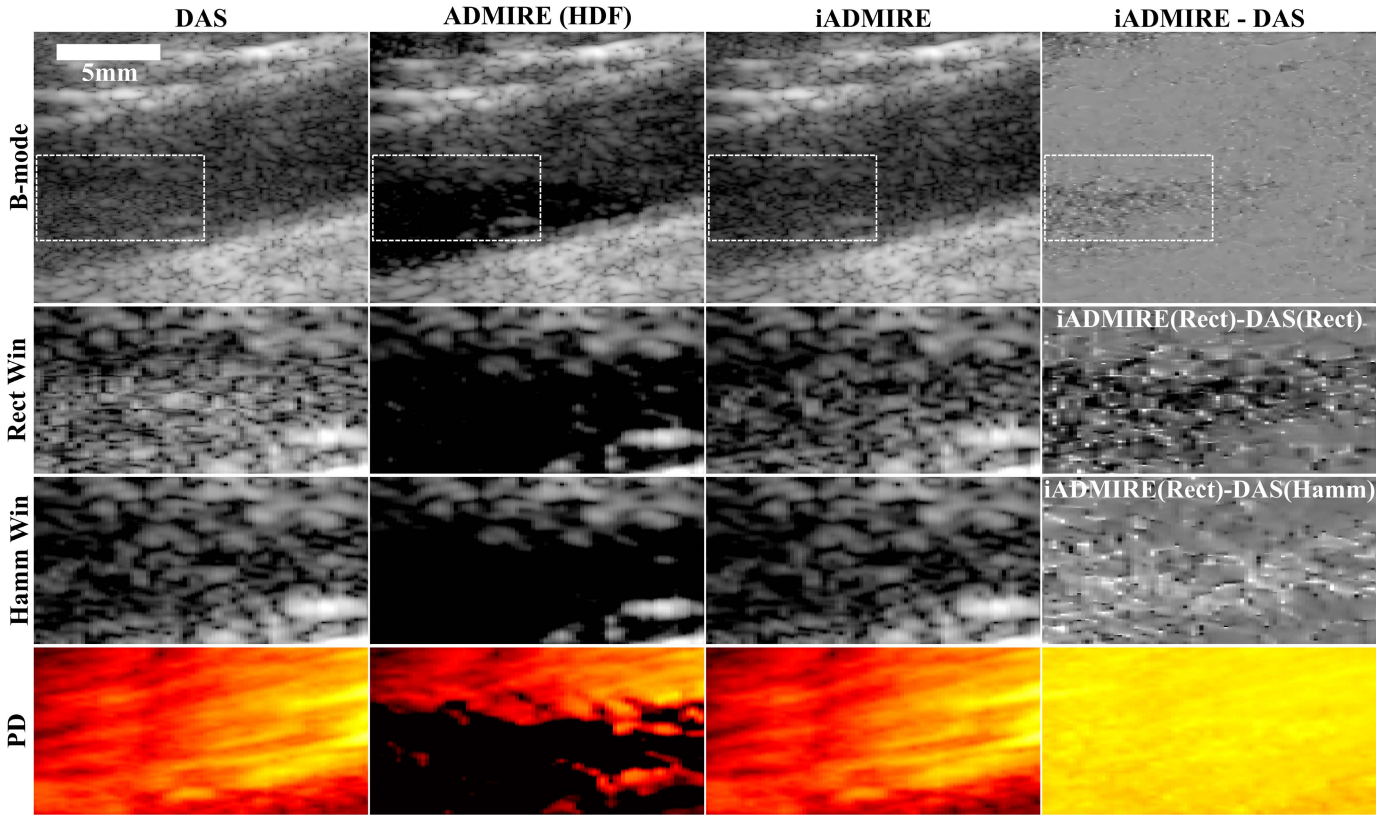

Fig. 10. DAS, ADMIRE (HDF), iADMIRE, and the difference between iADMIRE and DAS images from an *in vivo* carotid artery from a healthy individual. Top row: standard B-mode images on a 70-dB log scale. Middle and bottom rows: white dashed line section from the B-mode enlarged. Middle rows: the same B-mode on a narrower 30-dB log scale using rectangular (Rect) and Hamming (Hamm) apodization, respectively. Bottom row: PD images on a 25-dB log scale. The lower dynamic range helps to highlight the improved speckle texture in the iADMIRE B-mode image.

magnitudes appear identical on a more traditional compressed log scale. In the results, the dynamic range curves show that all beamformers eventually saturate for cysts above some level of contrast, both hyperechoic and hypoechoic, due to sidelobe clutter. In low reverberation clutter cases, iADMIRE is able to more accurately report the true contrast in the range of −40–60-dB cysts when compared with other beamformers, improving upon ADMIRE and DAS. ADMIRE (HDF) and iADMIRE perform well primarily due to their ability to mitigate the sidelobe artifact without introducing a dark region artifact. However, at higher levels of sidelobe clutter, ADMIRE (HDF) begins to struggle to preserve the true background speckle resulting in a dark region artifact, while iADMIRE is able to differentiate between the clutter and the background speckle more effectively.

We characterized the effect of the sidelobe artifact on the background speckle by computing the 2-D correlation coefficient for all methods at all levels of contrast against an untouched speckle background (no cyst or additional clutter). For hypoechoic cysts, the background region is unaffected since there is no strong acoustic target. However, for the strong acoustic cysts at 30 dB and greater, many of the beamformers begin to suffer reduced speckle accuracy. Only ADMIRE (HDF) and iADMIRE manage to maintain above 0.90 speckle accuracy at 50 dB, and only iADMIRE preserves speckle accurately at 60 dB. As with CRDR, speckle correlation drops significantly as the level of added reverberation clutter rises above the background speckle.

From the CNR results, SLSC is the clear choice if cyst detectability is the primary focus. Since SLSC takes advantage of the lack of coherence in the sidelobe clutter, it is able to dramatically reduce the amplitude of the background in those areas, increasing the contrast and decreasing the variance. GLT functions similar, though to a lesser extreme. All the other beamformers have similar performance, with DAS and the ADMIRE variants performing nearly identically. GCNR, on the other hand, only compares the probability distribution of the magnitudes of the cyst versus the background, meaning that given a fixed speckle variance, there is some level of contrast above which all cysts will have a GCNR of 1, regardless of beamformer. Because of this, GCNR does not value the difference in contrast or the speckle variance beyond a certain level, and therefore does not fully differentiate between beamformers in this study. The GCNR results argue that the improved CNR that SLSC and GLT are getting from suppressing the background is not functionally improving detectability more than the other beamformers, which is fair since the cysts are extremely easy to differentiate from the background, regardless of which method is used.

The added reverberation clutter results show that iADMIRE is better able to correctly mitigate sidelobe clutter for reverberation cases up to 0-dB SCR, but once the reverberation clutter

is sufficiently strong, it begins to fail along with the other beamformers. At −10- and −20-dB SCR, all of the beamformers failed to represent true cyst contrast due to the complete corruption of the background speckle. This indicates that ADMIRE is more robust to high levels of sidelobe clutter than reverberation clutter due to the nature of the two sources. Specifically, off-axis signals have intrinsically lower correlation with the ROI signals when compared with reverberation signals, which makes it more difficult to fully separate high amplitude reverberant sources [35]. This issue could potentially be avoided using tissue harmonic imaging, which has been demonstrated many times to reduce reverberation [31], [32], [36] and has previously been successfully implemented with ADMIRE [13].

When ADMIRE is tuned toward an L1 fit (encouraging sparsity of coefficients), the high magnitude signals (reverberation) are preferentially fit, and the weaker signals are lost. However, with a more L2 fit (encouraging more nonzero coefficients), the model again prefers the high frequency predictors to achieve a lower error fit to the input signal, resulting in the underlying signal being misclassified as clutter. For the severe reverberation clutter cases, iADMIRE requires many iterations to progressively remove the high magnitude components first without overfitting the ROI, but this causes compounding of small model fitting errors due to the many iterations.

B. Bright Scatterer Phantoms

Qualitatively, the bright scatterer phantom results show that ADMIRE and iADMIRE almost entirely mitigate the sidelobe artifact that is present in the DAS, DMAS, GCF, and MV images. Furthermore, iADMIRE mitigates the dark region artifact that begins to appear in ADMIRE (HDF) at 80 and 100 dB, restoring the lost background speckle. Not only is the magnitude of the speckle restored, but the 2-D correlation coefficient shows that it is restoring the speckle accurately. In the 100-dB bright scatterer case, iADMIRE reports a correlation coefficient of 0.93, with MV and DMAS a distant runner-up with coefficients of 0.42 and 0.40, respectively. Though none of the beamformers were able to perform well in the 120-dB bright scatterer case, this shows that iADMIRE is able to mitigate both sidelobe and dark region artifacts in cases up to 100 dB.

C. In Vivo Carotid Artery

The data obtained from the carotid artery shows an example of the dark region artifact *in vivo*. ADMIRE (HDF), in the presence of the sidelobe clutter from the tissue wall, completely removes the blood speckle along with the clutter, resulting in a complete loss of the blood signal in that region. In comparison, iADMIRE is able to restore that lost blood signal and largely preserve the underlying speckle, which can be seen by the improved speckle appearance in the highlighted cluttered region compared to DAS with rectangular apodization. Hamming apodization clearly helps to remove the clutter signal from the vessel, but seems to remove more signal compared to iADMIRE with rectangular apodization. Given the nature of the *in vivo* situation, it is difficult to know whether the Hamming apodization is removing too much signal or not.

VI. Conclusion

We have presented iADMIRE as a modification to the original ADMIRE algorithm that is able to extend its dynamic range as well as mitigate the dark region artifact that results from adaptive beamformers. Using CRDR and GCNR, we confirmed the performance of iADMIRE when compared with other common adaptive beamformers, while also demonstrating the issues with regard to sidelobe artifact saturation and true contrast.

In the no added reverberation clutter cases, iADMIRE had a CRDR of 72.1 dB, improving upon the next best methods DAS and ADMIRE (HDF) at 50.0 and 45.4 dB, respectively. The added reverberation clutter cases proved more difficult, where iADMIRE loses some of its relative improvements as the level of reverberation increases. This indicates that iADMIRE has difficulty fully differentiating these highly reverberant sources from the ROI signals. As Byram *et al.* [13] showed previously, the physical model of ADMIRE loses accuracy in the extreme near field and additionally sources at different depths from the ROI tend to have higher correlation with the ROI when compared with same-depth, off-axis sources [35]. This means that while iADMIRE is robust to off-axis clutter, differentiating between near-field and ROI signals is more of a challenge in these highly reverberant cases.

Acknowledgment

The authors would like to thank the staff of the Vanderbilt University ACCRE computing resource.

References

[1] G. Matrone, A. S. Savoia, G. Caliano, and G. Magenes, "The delay multiply and sum beamforming algorithm in ultrasound B-mode medical imaging," *IEEE Trans. Med. Imag.*, vol. 34, no. 4, pp. 940–949, Apr. 2015.

[2] P.-C. Li and M.-L. Li, "Adaptive imaging using the generalized coherence factor," *IEEE Trans. Ultrason., Ferroelectr., Freq. Control*, vol. 50, no. 2, pp. 128–141, Feb. 2003.

[3] B. M. Asl and A. Mahloojifar, "Minimum variance beamforming combined with adaptive coherence weighting applied to medical ultrasound imaging," *IEEE Trans. Ultrason., Ferroelectr., Freq. Control*, vol. 56, no. 9, pp. 1923–1931, Sep. 2009.

[4] O. M. H. Rindal, A. Austeng, H. Torp, S. Holm, and A. Rodriguez-Molares, "The dynamic range of adaptive beamformers," in *Proc. IEEE Int. Ultrason. Symp. (IUS)*, Sep. 2016, pp. 1–4.

[5] K. Dei, A. Luchies, and B. Byram, "Contrast ratio dynamic range: A new beamformer performance metric," in *Proc. IEEE Int. Ultrason. Symp. (IUS)*, Sep. 2017, pp. 1–4.

[6] A. Rodriguez-Molares, O. M. H. Rindal, J. D'Hooge, S.-E. Masoy, A. Austeng, and H. Torp, "The generalized contrast-to-noise ratio," in *Proc. IEEE Int. Ultrason. Symp. (IUS)*, Oct. 2018, pp. 1–4.

[7] A. Rodriguez-Molares *et al.*, "The generalized contrast-to-noise ratio: A formal definition for lesion detectability," *IEEE Trans. Ultrason., Ferroelectr., Freq. Control*, vol. 67, no. 4, pp. 745–759, Apr. 2019.

[8] O. M. H. Rindal, A. Austeng, A. Fatemi, and A. Rodriguez-Molares, "The effect of dynamic range alterations in the estimation of contrast," *IEEE Trans. Ultrason., Ferroelectr., Freq. Control*, vol. 66, no. 7, pp. 1198–1208, Jul. 2019.

[9] O. M. H. Rindal, A. Rodriguez-Molares, and A. Austeng, "The dark region artifact in adaptive ultrasound beamforming," in *Proc. IEEE Int. Ultrason. Symp. (IUS)*, Sep. 2017, pp. 1–4.

[10] G. Eknoyan, "A clinical view of simple and complex renal cysts," *J. Amer. Soc. Nephrol.*, vol. 20, no. 9, pp. 1874–1876, Sep. 2009.

[11] K. S. Warren and J. McFarlane, "The Bosniak classification of renal cystic masses," *BJU Int.*, vol. 95, no. 7, pp. 939–942, May 2005.
[12] C. L. Siegel, E. G. McFarland, J. A. Brink, A. J. Fisher, P. Humphrey, and J. P. Heiken, "CT of cystic renal masses: Analysis of diagnostic performance and interobserver variation," *Amer. J. Roentgenol.*, vol. 169, pp. 813–818, Sep. 1997.
[13] B. Byram, K. Dei, J. Tierney, and D. Dumont, "A model and regularization scheme for ultrasonic beamforming clutter reduction," *IEEE Trans. Ultrason., Ferroelectr., Freq. Control*, vol. 62, no. 11, pp. 1913–1927, Nov. 2015.
[14] K. Dei and B. Byram, "The impact of model-based clutter suppression on cluttered, aberrated wavefronts," *IEEE Trans. Ultrason., Ferroelectr., Freq. Control*, vol. 64, no. 10, pp. 1450–1464, Oct. 2017.
[15] B. Byram and M. Jakovljevic, "Ultrasonic multipath and beamforming clutter reduction: A chirp model approach," *IEEE Trans. Ultrason., Ferroelectr., Freq. Control*, vol. 61, no. 3, pp. 428–440, Mar. 2014.
[16] K. Dei and B. Byram, "A robust method for ultrasound beamforming in the presence of off-axis clutter and sound speed variation," *Ultrasonics*, vol. 89, pp. 34–45, Sep. 2018.
[17] H. Zou and T. Hastie, "Regularization and variable selection via the elastic net," *J. Roy. Stat. Soc. B, Stat. Methodol.*, vol. 67, no. 2, pp. 301–320, Apr. 2005.
[18] R. J. Tibshirani and J. Taylor, "Degrees of freedom in lasso problems," *Ann. Statist.*, vol. 40, no. 2, pp. 1198–1232, Apr. 2012.
[19] B. Yang, "A study of inverse short-time Fourier transform," in *Proc. IEEE Int. Conf. Acoust., Speech Signal Process.*, Mar. 2008, pp. 3541–3544.
[20] K. Dei, S. Schlunk, and B. Byram, "Computationally efficient implementation of aperture domain model image reconstruction," *IEEE Trans. Ultrason., Ferroelectr., Freq. Control*, vol. 66, no. 10, pp. 1546–1559, Oct. 2019. [Online]. Available: https://ieeexplore.ieee.org/document/8746209/
[21] S. Schlunk, K. Dei, and B. Byram, "Iterative ADMIRE for high dynamic range B-mode," in *Proc. IEEE Int. Ultrason. Symp. (IUS)*, Oct. 2018, pp. 1–4.
[22] I. K. Holfort, F. Gran, and J. A. Jensen, "Broadband minimum variance beamforming for ultrasound imaging," *IEEE Trans. Ultrason., Ferroelectr., Freq. Control*, vol. 56, no. 2, pp. 314–325, Feb. 2009.
[23] J. F. Synnevag, A. Austeng, and S. Holm, "Adaptive beamforming applied to medical ultrasound imaging," *IEEE Trans. Ultrason., Ferroelectr., Freq. Control*, vol. 54, no. 8, pp. 1606–1613, Aug. 2007.
[24] M. A. Lediju, G. E. Trahey, B. C. Byram, and J. J. Dahl, "Short-lag spatial coherence of backscattered echoes: Imaging characteristics," *IEEE Trans. Ultrason., Ferroelectr., Freq. Control*, vol. 58, no. 7, pp. 1377–1388, Jul. 2011.
[25] R. Mallart and M. Fink, "The van Cittert–Zernike theorem in pulse echo measurements," *J. Acoust. Soc. Amer.*, vol. 90, no. 5, pp. 2718–2727, Nov. 1991.
[26] M. A. L. Bell, J. J. Dahl, and G. E. Trahey, "Resolution and brightness characteristics of short-lag spatial coherence (SLSC) images," *IEEE Trans. Ultrason., Ferroelectr., Freq. Control*, vol. 62, no. 7, pp. 1265–1276, Jul. 2015.
[27] J. A. Jensen, "FIELD: A program for simulating ultrasound systems," in *Proc. 10th Nordic-Baltic Conf. Biomed. Imag. Published Med. Biological Eng. Comput.*, vol. 34, 1996, pp. 351–353.
[28] J. A. Jensen and N. B. Svendsen, "Calculation of pressure fields from arbitrarily shaped, apodized, and excited ultrasound transducers," *IEEE Trans. Ultrason., Ferroelectr., Freq. Control*, vol. 39, no. 2, pp. 262–267, Mar. 1992.
[29] B. Byram and J. Shu, "Pseudononlinear ultrasound simulation approach for reverberation clutter," *J. Med. Imag.*, vol. 3, no. 4, Dec. 2016, Art. no. 046005.
[30] B. Byram and J. Shu, "A pseudo non-linear method for fast simulations of ultrasonic reverberation," *Proc. SPIE*, vol. 9790, pp. 1–7, Apr. 2016.
[31] G. F. Pinton, G. E. Trahey, and J. J. Dahl, "Sources of image degradation in fundamental and harmonic ultrasound imaging using nonlinear, full-wave simulations," *IEEE Trans. Ultrason., Ferroelectr., Freq. Control*, vol. 58, no. 4, pp. 754–765, Apr. 2011.
[32] A. Fatemi, E. A. R. Berg, and A. Rodriguez-Molares, "Studying the origin of reverberation clutter in echocardiography: *In vitro* experiments and *in vivo* demonstrations," *Ultrasound Med. Biol.*, vol. 45, no. 7, pp. 1799–1813, Jul. 2019.
[33] M. A. Lediju, M. J. Pihl, J. J. Dahl, and G. E. Trahey, "Quantitative assessment of the magnitude, impact and spatial extent of ultrasonic clutter," *Ultrason. Imag.*, vol. 30, no. 3, pp. 151–168, Jul. 2008.
[34] G. Montaldo, M. Tanter, J. Bercoff, N. Benech, and M. Fink, "Coherent plane-wave compounding for very high frame rate ultrasonography and transient elastography," *IEEE Trans. Ultrason., Ferroelectr., Freq. Control*, vol. 56, no. 3, pp. 489–506, Mar. 2009.
[35] B. Byram, J. Shu, and K. Dei, "Nonlinear beamforming of aperture domain signals," in *Proc. IEEE Int. Ultrason. Symp. (IUS)*, Oct. 2015, pp. 1–6.
[36] S. Choudhry *et al.*, "Comparison of tissue harmonic imaging with conventional US in abdominal disease," *RadioGraphics*, vol. 20, no. 4, pp. 1127–1135, 2000.

Siegfried Schlunk (Graduate Student Member, IEEE) grew up at Nashville, TN, USA. He received the B.E. degree in biomedical engineering and mathematics from Vanderbilt University, Nashville, in 2016, where he is currently pursuing the Ph.D. degree in biomedical engineering.

His research interest focuses on developing methods for improving ultrasound image quality in cardiac and kidney applications.

Kazuyuki Dei was born and raised in Saitama, Japan. He received the B.S. degree in mechanical engineering from the University of California, Berkeley, CA, USA, in 2000, and the Ph.D. degree in biomedical engineering from Vanderbilt University, Nashville, TN, USA, in 2019.

He was with Fujitsu Ltd., Tokyo, Japan, and with Fujitsu Semiconductor America Inc., Sunnyvale, CA, USA, as an Electrical Design and Development Engineer over 12 years. His research interests include model-based acoustic clutter suppression, phase-aberration measurements, beamforming, and signal and image processing.

Brett Byram (Member, IEEE) received the B.S. degree in biomedical engineering and mathematics from Vanderbilt University, Nashville, TN, USA, in 2004, and the Ph.D. degree in biomedical engineering from Duke University, Durham, NC, USA.

He then stayed as a Research Assistant Professor with Duke University. In 2013, he joined the Biomedical Engineering Department, Vanderbilt University, as an Assistant Professor. He has spent time working in the Jørgen Jensen's Center for Fast Ultrasound, Lyngby, Denmark, and also in the Siemens Healthcare's Ultrasound Division, Mountain View, CA, USA. He currently runs the Biomedical Elasticity and Acoustic Measurement (BEAM) Laboratory, where he and others in the lab pursue solutions to clinical problems using ultrasound. He is also with the Vanderbilt Institute for Surgery and Engineering (VISE) and the Vanderbilt University Institute of Imaging Science (VUIIS). His research interests include beamforming, motion estimation, and other related signal processing and hardware development tasks.